Reptile-like physiology in Early Jurassic stem-mammals

Elis Newham, Pamela G. Gill, Philippa Brewer, Michael J. Benton, Vincent Fernandez, Neil J. Gostling, David Haberthür, Jukka Jernvall, Tuomas Kankanpää, Aki Kallonen, Charles Navarro, Alexandra Pacureanu, Berit Zeller-Plumhoff, Kelly Richards, Kate Robson-Brown, Philipp Schneider, Heikki Suhonen, Paul Tafforeau, Katherine Williams, & Ian J. Corfe.

Despite considerable advances in knowledge of the anatomy, ecology and evolution of early mammals, far less is known about their physiology. Evidence is contradictory concerning the timing and fossil groups in which mammalian endothermy arose. To determine the state of metabolic evolution in two of the earliest stem-mammals, the Early Jurassic *Morganucodon* and *Kuehneotherium*, we used separate proxies for basal and maximum metabolic rate. We show, using synchrotron X-ray tomographic imaging of incremental tooth cementum, that they had maximum lifespans considerably longer than comparably sized living mammals, but similar to those of reptiles, and so they likely had reptilian-level estimates of basal metabolic rate. Measurements of femoral nutrient foramina show *Morganucodon* had blood flow rates intermediate between living mammals and reptiles, suggesting maximum metabolic rates increased evolutionarily before basal metabolic rates. Stem mammals lacked the elevated endothermic metabolism of living mammals, highlighting the mosaic nature of mammalian physiological evolution.

Recent discoveries and analyses have revolutionized our knowledge of Mesozoic mammals, revealing novel aspects of their ecology[1,2,] development[2,3], systematics[2,3] and macroevolution[4,5]. However, details of physiology are more difficult to determine from

fossils, and our knowledge of physiological evolution remains comparatively poor. Living mammals are endotherms, possessing the ability to control and maintain metabolically produced heat, and have a substantially higher capacity for sustained aerobic activity than ectothermic animals[6-8]. The origin of endothermy is an important event in mammalian evolution, often noted as key to their success[6-8]. There are a number of competing evolutionary hypotheses for the origin of endothermy: (a) selection for higher maximum metabolic rates (MMR) enhanced sustained aerobic activity[6,9,10]; (b) selection for higher basal metabolic rates (BMR) enhanced thermoregulatory control[11,12]; or (c) MMR and BMR evolved in lockstep with each other[7,8].

Direct evidence from living mammals to support these hypotheses is equivocal[7]. Recent analyses find no long-term evolutionary trend in BMR[13] contradicting earlier suggestions of increasing BMR throughout the Cenozoic[12], and so implying that the Middle Jurassic (~170 Ma) most recent common ancestor (MRCA) of living mammals[13] possessed a BMR within the range of present-day mammals. Several indirect indicators of metabolic physiology in fossil synapsids have been suggested but provide contradictory evidence for the timing of the origin of endothermy and its evolutionary tempo. These include: the presence of fibrolamellar long-bone histology[14,15], first seen in the Early Permian synapsid *Ophiacodon* ~300 million years (Ma) ago[16]; the presence of an infraorbital canal and lack of parietal foramen, used to infer facial whiskers, fur, lactation and endothermy in Early Triassic (~245 Ma) cynodonts[17]; inferred maxillary nasal turbinates in the Late Permian (~255 Ma) therapsid *Glanosuchus*, used to suggest that mammalian levels of endothermy evolved by the Late Triassic (~210 Ma)[18]; a trend toward increased relative brain size initiated in Late Triassic non-mammaliaform cynodonts[19] and the mammaliaform (stem mammal *sensu* Rowe[20]) *Morganucodon*[21,22]; and acquisition of a parasagittal gait in the Early Cretaceous (~125 Ma) therian mammals *Eomaia* and *Sinodelphys*[23]. Several recent studies provide more

quantitative links to physiological parameters. Oxygen isotopes were used to infer elevated thermometabolism in Middle-Late Permian (~270-255 Ma) eucynodonts[24]; red blood cell size diminution in Late Permian (~255 Ma) eutheriodontid therapsids was linked via two proxies to increased MMR[25]; and osteocyte lacuna shape correlations suggested 'mammalian' resting metabolic rates in Permo-Triassic (~250 Ma) dicynodonts[26].

However, the inconsistency of these characters, in time and with respect to phylogeny[27,28], along with re-assessments of function in relation to endothermy[7,29,30], limit their use as conclusive indicators of modern mammalian levels of endothermy in fossil taxa. Such temporal and phylogenetic heterogeneity suggests that the evolution of mammalian endothermy followed a complex, mosaic pattern with different physiological aspects likely evolving independently, and at separate rates, towards current mammalian levels. Additionally, few of these physiological proxies are directly related to measurable aspects of metabolic rate.

To address these issues, we used two proxies to improve understanding of physiology at one of the most important nodes along this transition by estimating BMR and growth rate, and calculating a known proxy for MMR, for two of the earliest known mammaliaforms, *Morganucodon* and *Kuehneotherium*[1,31].

Lifespan: a proxy for mammaliaform physiology

We used maximum lifespan (i.e. the single longest known lifespan of a taxon) estimates for fossil mammaliaform taxa as a proxy for both BMR[32] and postnatal growth rate[33]. In extant tetrapods, negative correlations exist between maximum lifespan and BMR[32], and maximum lifespan and growth rate[33,34]. In general, the longer a mammal's lifespan, the lower its size-adjusted BMR and growth rate. Growth rates have been shown to correlate strongly with metabolic power in extant vertebrates, with endotherms growing an order of magnitude faster

than ectotherms[34,35]. Maximum lifespan is an applicable value for fossil samples, as unlike

other metrics (e.g. 10% most long-lived or mean lifespan of a cohort) it does not rely on

cohort- or population-based statistics that fossil samples cannot fulfil[36]. This value is also less

susceptible to extrinsic population-level factors on lifespan, such as disease or predation, and

relates most closely to the physiological limit of lifespan of an organism. An accurate

assessment of maximum lifespan in fossil mammals can therefore be used to estimate their

metabolic potential.

To estimate mammaliaform lifespans we used cementochronology. This well-

established technique, which counts annual growth increments in tooth root cementum, has

been used to record lifespans in extant mammals[37] with over 70 species aged using this

technique[38]. Cementum is a mineralized dental tissue surrounding the tooth root (Fig. 1a, b),

attaching it to the periodontal ligament and anchoring the tooth within the alveolus[37]. Growth

of cementum is continuous throughout life in extant mammals and seasonally appositional in

nature, forming a series of increments of differing thickness and opacity when viewed in

histological thin-sections under light microscopy. The correlation between increment count

and chronological age is well documented, with one thick and one thin increment deposited

every year[38]. It has been shown that the thin, hyper-mineralized opaque increments record

growth rate reduction in less favourable seasons[39,40].

Despite this potential, cementochronology has not previously been attempted for

fossil mammals older than the Pleistocene (2.6 Ma)[41] because histological thin-sections

destroy fossils and provide only a restricted field-of-view. We overcame these problems by

using propagation phase-contrast X-ray synchrotron radiation microtomography (PPC-

SRμCT) to non-destructively image fossilized cementum increments[42,43]. The sub-

micrometre resolution, fast-throughput and three-dimensional (3D) nature of PPC-SRμCT

allows for large sample sizes and for increments to be imaged along their entire transverse

and longitudinal trajectories in volumetric PPC-SRµCT datasets. Cementum increments are known to occasionally split and coalesce, creating errors in counts based on single, or limited numbers of, two-dimensional thin sections created for each tooth[37,44] (SI Fig. 1). PPC-SRµCT imaging and 3D segmentation of individual increments across extensive vertical distances within the cementum allowed us to confidently distinguish principal annual increments from any accessory increments created by lensing and coalescence (see Methods).

Morganucodon and *Kuehneotherium* are shrew-sized insectivores[1,45], which co-existed on a small landmass during the Early Jurassic marine transgression (Hettangian-early Sinemurian, ~200 Ma) in what is now Glamorgan, South Wales, UK[46]. Thousands of their bones and teeth were washed into karst fissures that have subsequently been revealed by quarrying. This provides a rare opportunity to analyse large samples of fossil material needed for confident estimation of maximum lifespan. Importantly, these are the earliest diphyodont taxa (Fig. 2), with a single replacement of non-molar teeth and no molar tooth replacement[31], and so estimates of lifespan are accurate to the time of the measured tooth root formation.

The fossil sample studied included both isolated teeth, and mandibles, with multiple teeth or roots *in-situ*. We applied PPC-SRµCT to 87 *Morganucodon* specimens (52 isolated teeth, 35 dentaries, all *M. watsoni*), and 119 *Kuehneotherium* specimens (116 isolated teeth, 3 dentaries) (see Methods). From these, 34 *Morganucodon* and 27 *Kuehneotherium* specimens were sufficiently well preserved for three observers to independently estimate lifespan from cementum increments. These estimates were compared to validate their accuracy and precision (see Methods) (SI Table 1). The remainder showed physical and/or diagenetic damage that prevented increment measurement (SI Fig. 2).

The cementum of *Morganucodon* and *Kuehneotherium* (Fig. 1a, b) is distinguished from dentine in our PPC-SRµCT data by a distinct boundary layer separating the two tissues. This lies external to the granular layer of Tomes of the dentine and is interpreted as the

hyaline layer of Hopewell-Smith (Fig. 1c–g). Synchrotron nanotomographic imaging (30 nm isotropic voxel size) highlights individual Sharpey's fibre bundles (linking cementum to the periodontal ligament in extant mammals) visible in several exceptionally preserved specimens which can be traced radially through the cementum (Fig. 1g). Across the tooth-root transverse axis, cementum is ~10-70 μm radial thickness and displays a series of contrasting light and dark circumferential increments representing different material densities (Figs. 1e–g, 3a–d). Higher density increments (represented by greater greyscale values) are on average 2–3 μm radial thickness, and lower density increments are 1–3μm radial thickness (Figs. 1c–g, 3a–d). Individual increments can be followed continuously both longitudinally and transversely through the entire scanned volume of a tooth root (Fig. 3e, f).

Cementum increment accuracy, tooth eruption sequence and timing

We tested the accuracy of cementum increment counts for predicting lifespan in fossils by additional PPC-SRµCT imaging and counting of increments in the cementum of several teeth along the tooth row in eight dentulous *Morganucodon* specimens with a range of teeth *in-situ* (Table 1), and of growth increments (Lines of Arrested Growth; LAGs) in the periosteal region of the dentary bone in two of these (Fig. 4). In both specimens where dentary LAGs are found, counts are identical with the cementum increments in the teeth (p3- m2) (Fig. 4). Also, comparisons between counts of cementum increments are identical across all four premolars (p1- 4) and the anterior molars (m1-2), in all specimens where they occur together (Table 1). This agreement between p1–m2 teeth and dentary increment counts indicates that growth in both teeth and jaws was following the same, circum-annual rhythm, as previously reported for multiple extant mammals species[37]. We consider this to be strong support for the accuracy of lifespan estimates based on these increment counts.

The increment counts along *Morganucodon* dentary toothrows can also provide information on eruption sequence and timing (see SI for more details). The first permanent premolar to the second molar all erupted within one year, with the first molar erupting prior to the third and fourth premolars (NHMUK PV M 27312; see SI for more details). The ultimate incisor (i4), the canine, and the third molar erupted in the following year. We do not have information on eruption timing of more anterior incisors, or the fourth molar, and the fifth molar is only occasionally present. As we estimate *Morganucodon* was long lived relative to comparatively sized extant mammals (see below), this pattern of most of the adult tooth row being in place during the first two years of life is also supportive of a relatively short (compared with its total lifespan) juvenile stage[47], and determinate growth as previously suggested[48]. The absolute length of these stages in *Morganucodon* is however considerably longer than extant mammals of comparable body size[37]. Unfortunately, dentulous specimens of *Kuehneotherium* are rare, and there are no tooth rows with cementum increment counts in our sample.

Long lifespans, low BMR and growth rates

Cementum increment counts provide a minimum estimate of maximum lifespan of 14 years for *Morganucodon*, and nine years for *Kuehneotherium* (Figs 3, 5a). These may underestimate true maximum lifespan, as any damage to outer cementum increments would reduce estimated maximum lifespan. One-way ANOVA comparisons of mean intra-observer coefficient of variation (*CV*) between our study and ten previous cementochronological studies of different extant mammal species (see Methods) with similar age ranges suggest that values for PPC-SRµCT data (Shapiro-Wilk *W* = 1) of *Morganucodon* (*CV* = 9.32) and *Kuehneotherium* (*CV* = 4.89) are significantly lower than previous thin section-based studies

($W = 0.93$; minimum extant $CV = 14.2$, mean $CV = 21.8$, standard deviation = 5.87) ($F = 11.12$, $p < 0.01$) (SI Table 3).

We estimated body mass ranges of 10.7–25.0 g (mean 17.9 g) for *Morganucodon* and 14.9–32.7 g (mean 23.8 g) for *Kuehneotherium* (minimum mass estimates based on skull length[21] and maximum mass estimates on dentary length[45]; see Methods). Maximum lifespan and mean body mass for the mammaliaforms were compared with published data for large samples of terrestrial, non-volant wild extant mammal (n = 278) and non-avian reptile (n = 256) species (Methods; SI Table 5). Maximum wild lifespans of extant taxa were chosen for comparison with our fossil taxa as these values are the closest analogue to our estimated lifespans, relative to captive lifespan values. To ensure robustness of our results, we additionally analysed maximum captive lifespans of extant taxa below 100 g, which show an average increase above maximum wild lifespans of approximately 3.43 and 4.38 years per taxon, for mammals and reptiles respectively (SI figure 4). Broad results of statistical tests and the overall conclusions of our study are unchanged regardless of whether wild or captive data is used (see SI for analysis and further discussion of comparisons between our fossil lifespans and captive lifespans of extant taxa).

Phylogenetic generalised least squares (PGLS) regression of $\log_{10}$ transformed values shows that the fossil mammaliaforms fall within the range of extant reptiles and have longer maximum lifespans for their size, and are further above the mammal regression mean, than all extant mammals under 4 kg (the long-lived and secondarily dwarfed[49] mouse lemur *Microcebus murinus* is closest). Only the short-beaked echidna *Tachyglossus aculeatus*, a monotreme with long lifespan and low metabolic rate, exceeds the distance above the mammalian mean for *Kuehneotherium*, but not *Morganucodon* (Fig. 5b). One-way phylogenetic ANCOVA comparisons show that regression slopes for extant mammals and reptiles are statistically similar ($p = 0.35$) but their means are significantly separated ($p =$

0.036), with reptiles on average living 18.3 years longer than mammals of the same body mass.

To estimate BMR, we used PGLS and recovered significant correlations between $\log_{10}$ transformed values of maximum wild lifespan and mass-specific standard metabolic rate (msSMR; measured in mL.O_2.hr^{-1}.g^{-1} and analogous with BMR in extant mammals – SMR was used as BMR cannot be measured in reptiles[50]) from published data for 117 extant mammals and 55 extant reptiles (Methods; SI Table 5) (Fig. 6a). Using the correlation between maximum wild reptile lifespan and msSMR and plotting our mammaliforms directly onto this regression line we estimated a reptile-derived msSMR of 0.055 mL.O_2.hr^{-1}.g^{-1} (*Morganucodon*) and 0.08 mL.O_2.hr^{-1}.g^{-1} (*Kuehneotherium*) (Fig. 6a). We additionally used the correlation between maximum wild mammal lifespan and msSMR and estimated a mammal-derived msSMR of 0.36 mL.O_2.hr^{-1}.g^{-1} for *Morganucodon* and 0.46 mL.O_2.hr^{-1}.g^{-1} for *Kuehneotherium* (Fig. 6a)*. When $\log_{10}$ PGLS is used to regress these estimates against body mass, both mammaliaforms fall outside the 95% predictor interval (PI) of the mammalian data and within the reptile range of msSMR, regardless of whether mammaliaform msSMR is estimated from reptilian or mammalian data (Fig. 5c). This suggests the mammaliaforms had significantly lower msSMR values compared to extant mammals of similar size. The comparably sized mammal (<100 g) of lowest msSMR is the marsupial *Dasycercus cristicauda*, with a maximum wild lifespan of seven years and msSMR of 0.63 mL.O_2.hr^{-1}.g^{-1} (Fig. 5c).

We estimated growth rates using PGLS correlations between maximum wild lifespan and growth rate[33,34] from published data from 115 extant mammals and 30 extant reptiles (Methods; SI Table 5) (Fig. 6b). From mammal data we estimate growth rate constants K (days^{-1} - see Methods) of 1.085^{-2} days^{-1} (*Morganucodon*) and 1.474e^{-2} days^{-1} (*Kuehneotherium*). From reptile data we estimated K = 4.91^{-4} days^{-1} (*Morganucodon*) and K

= 6.65^{-4} days^{-1} (*Kuehneotherium*) (Fig 6b). Log$_{10}$ PGLS regression against body mass again places both mammaliaforms outside the mammalian 95% PI and within the reptile growth rate range, whether estimated from mammalian or reptilian data (Fig. 5d). The lowest growth rate of any <100g extant mammal is $K = 3.24e^{-2}$ days^{-1} for the Mongolian gerbil *Meriones unguiculatus*.

In summary, our estimates of maximum lifespan provided by tomographic imaging of cementum increments in *Morganucodon* and *Kuehneotherium* are significantly longer than the maximum wild lifespan of any extant mammal of comparable body mass. These lifespans provide estimates of SMR/BMR and growth rate that are significantly lower than comparably sized extant mammals, and instead correspond to those of extant reptiles.

Femoral blood-flow shows intermediate MMR

To compare our fossil mammaliaform BMR estimates with MMR, we used a second proxy directly linked to MMR[51]. The ratio between nutrient foramen area and femur length has been used as an index for relative blood flow (Q_i) through the femur during and after metabolically demanding exercise ($Qi = r_f^A/L$; where r_f = foramen radius and L = femur length), previously shown to correlate well with MMR[51]. From micro-computed tomography (μCT) data of the six most complete *Morganucodon* femoral diaphyses available, we segmented all nutrient foramina (Fig. 7a) and estimated their area by measuring their minimal radii (see Methods). *Kuehneotherium* could not be included as no suitable femoral specimens are known.

We estimated a Q_i of 3.829e^{-7} mm^3 for *Morganucodon* and compared this with published and new data (Methods) for extant mammals (n = 69) and reptiles (n = 30). The latter includes varanids (n = 8) which in the absence of mammalian predators fill an active hunting niche and tend to have mammalian MMR levels while retaining reptilian BMR levels[51] (SI Table 4). One-way ANCOVA comparisons show that means of GLS regression

slopes for extant mammals and non-varanid reptiles are significantly different ($p < 0.01$) while the slopes are similar ($p = 0.16$). Log_{10} GLS regression of body mass and Q_i shows that *Morganucodon* is further above (higher Q_i for its mass) the non-varanid reptile mean than all non-varanid reptiles (phylogenetically informed statistical comparisons were not used here due to the non-significant lambda values showing no phylogenetic signal in the taxa used, see Methods). However, *Morganucodon* is also slightly further from the mammalian mean than the non-varanid reptile mean, and considerably closer to small non-varanid reptile species data points than those of small mammalian species (Fig. 7b). This intermediate Q_i, and so inferred intermediate MMR, suggests that while retaining typical reptilian BMR and growth rates, *Morganucodon* had MMR above non-varanid reptiles, but not as high as mammals or actively foraging varanid reptiles.

Discussion

We have used two quantitative proxies to determine the metabolic status of early mammaliaforms. Relatively long lifespans for both *Morganucodon* and *Kuehneotherium* result in SMR/BMR and growth rate estimates equivalent to modern reptiles of comparable size, and indeed at the higher lifespan/lower BMR/slower growth end of the reptile scale for *Morganucodon*. This is true whether we compare our fossil estimates to wild lifespans of extant taxa, or estimate their 'captive' lifespans and compare them to captive values for extant taxa. In contrast, femoral blood flow estimates (Q_i) suggest that the MMR of *Morganucodon* was intermediate between extant non-varanid reptiles and mammals. We therefore infer that in *Morganucodon* increased MMR (and so also absolute aerobic capacity, AAC = MMR - BMR) was initially selected for before BMR, and that the MMR-first hypothesis[6] is the best-supported model for the evolution of mammalian endothermy. We suggest that at least *Morganucodon*, if not also *Kuehneotherium*, occupied a metabolic grade

approaching extant varanids; able to undergo longer bouts of aerobically demanding activity than non-varanid reptiles, but not capable of sustaining either mammalian levels of aerobic activity or the elevated thermometabolism exhibited by living endotherms.

Evidence from non-mammalian synapsids (including changes in gait[7], long bone histology[15], and development of secondary osteological features correlated with increased metabolic rate[17,18]) indicate unquestionable changes in physiology from pelycosaur- to mammaliaform-grade taxa. Determinate growth[48] and reduction of dental replacement (diphyodonty) in basal mammaliaforms permitted more precise occlusion, which has been considered a key innovation in the development of mammalian endothermy through enabling increased assimilation and higher metabolism[52]. However, determinate growth and diphyodonty appear to have preceded the appearance of modern mammalian levels of endothermy, at least in *Morganucodon* and *Kuehneotherium*. We therefore suggest that the development of precise occlusion in basal mammaliaforms may be more associated with dietary specialization and niche partitioning[1].

Comparison of our results to those of other recent studies of physiology in fossil synapsids supports the hypothesis of a complex, mosaic pattern for the evolution of endothermy, with different characters being selected for at different rates through time and with respect to phylogeny. For example, the size diminution associated with the cynodont-mammaliaform transition[53] may have reversed the evolutionary trajectory of some previous histological proxies for endothermy[54], contributing to the complex, contradictory patterns observed. Our study also suggests more work is needed to compare fossil and extant ecto- and endo-thermic taxa directly in order to better understand their relative metabolic properties. Many previous studies rely on simple binary divisions, such as the presence/absence of fibrolamellar bone and/or respiratory nasal turbinates. These proxies cannot represent accurately the complex series of physiological characteristics that range

between 'ectothermy' and 'endothermy', and are frequently distributed homoplastically across the synapsid phylogeny, individually and with respect to each other. Other studies provide relative data such as preserved apatite oxygen isotopes[24] that allow comparisons with co-habiting ectothermic taxa but cannot be directly compared to extant data and so do not suggest where the studied fossil taxa fall in the metabolic spectrum of extant vertebrates. However, our results are compatible with recent work on living mammals, suggesting the BMR of the Middle Jurassic (~170 Ma) mammalian most recent common ancestor (MRCA) was comparable to present-day values[13]. This indicates evolution towards modern-day mammalian endothermy occurred during the 25 million year-long Early Jurassic, and suggests the mammalian mid-Jurassic adaptive radiation[4,5] was driven by this, or vice versa.

In conclusion, our data offer a direct link to measurable aspects of endothermy, such as basal (BMR) and maximum metabolic rate (MMR), at a key point in mammalian evolution. Further work applying these methods to additional Mesozoic mammaliaforms and mammals, and comparison with evidence from other physiological characteristics, will allow the evolutionary tempo and mode of multiple aspects of mammalian physiology to be determined. The early mammaliaforms *Morganucodon* and *Kuehneotherium* possessed surprisingly low, reptile-like metabolic rates, plus a mixture of plesiomorphic and derived characters[7] relating to life history and physiology. Ultimately, we can no longer assume that the endothermic metabolism of living mammals had evolved in the earliest mammaliaforms.

Methods

Choice of fossil specimens

All *Morganucodon* and *Kuehneotherium* specimens are from the Early Jurassic St Brides Island fissure suite, from Glamorgan, South Wales (UK)[1,55,56]. *Morganucodon* and *Kuehneotherium* specimens used for the cementum analysis are from the collections of the Natural History Museum, London, UK (NHMUK) and the *Morganucodon* femora specimens are from the collections of University Museum of Zoology Cambridge, UK (UMZC). The *Morganucodon* specimens are all one species, *Morganucodon watsoni,* from Pontalun 3 fissure in Pontalun quarry (now known as Lithalun), which was excavated in 1962-1963[46,55]. *Kuehneotherium* is not abundant in Pontalun 3 fissure and the specimens used for cementum analysis are from three Glamorgan fissures in Pontalun and Pant quarries; Pontalun 3, Pant 2 and Pant 4. Pontalun 3 and Pant 2 fissures have a relatively impoverished fauna, and Pant 4 has a more diverse biota[46]. *Kuehneotherium* from Pontalun 3 fissure is *Kuehneotherium praecursoris*[56], but those from the Pant fissures are considered to be different species, based on small molar differences[57]. All specimens from Pontalun 3 fissure in the Natural History Museum, London (*Morganucodon* and *Kuehneotherium*) were prepared by immersing dried blocks of clay matrix in hot tap water, with the addition of dilute hydrogen peroxide or sodium hexametaphosphate (Calgon) if required, but those in the UMZC collection were prepared with 10% acetic acid. *Kuehneotherium* specimens from Pant quarry (Pant 2 and Pant 4) were collected by the Kermack team from University College London, between 1955 and 1978, and are from a harder matrix which was prepared with 15% acetic acid[57].

The *Morganucodon* and *Kuehneotherium* specimens used for cementum analysis are either isolated teeth, or dentary specimens with a range of teeth *in-situ.* The lower dental formula of *Morganucodon* is i4: c1: p4; m4-5 and for *Kuehneotherium* it is i?: c1: p6: m6[1]. In *Morganucodon* the majority of isolated teeth measured were lower second molars (m2)

since they are easily identified, are relatively large, have robust separated roots, and, as anterior diphyodont molars, they should erupt relatively early and are not replaced, therefore offering a near-complete record of life history. However, i4, c, p3, p4, m1, m3, and m4 teeth were also studied in dentulous *Morganucodon* specimens. *Kuehneotherium* is not abundant from Pontalun 3 fissure, and so specimens were also selected from two Pant quarry fissures, Pant 2 and Pant 4, and all appropriate teeth were chosen; p5, p6, and a range of lower and upper molars[57]. Dentulous *Kuehneotherium* specimens are extremely rare and so isolated teeth were scanned in almost all cases.

Tomographic imaging of cementum

Pilot scans of two *Morganucodon* lower second molars (NHMUK PV M 104131 and NHMUK PV M 104132) were carried out in 2011 on the nanotomography imaging beamline ID22 at the European Synchrotron Radiation Facility (ESRF), Grenoble, France (project EC 1064). For ID22 we used the following experimental settings for computed tomographic (CT) imaging: X-ray energy of 29.6 keV, 1999 projections over a 180⁰ rotation, 0.5 ms exposure time, 321 nm voxel size, 405 mm sample-to-detector distance, diamond window, a 20 µm thick LSO scintillator doped with Tb, and 1.5 mm Al filter, single propagation distance tomography.

During a four-day experiment at the ID19 beamline of the ESRF (18/04/2014-22/04/2014), 71 additional *Morganucodon* specimens (52 isolated teeth and 19 dentaries) and two pilot *Kuehneotherium* specimens were scanned (project ES 152). A single harmonic U13 undulator was used as the X-ray source, delivering a pink X-ray beam with peak energy at 26.5 keV, with a 1.4 mm Al filter used to cut the background lower energies. The detector was a microscope optic system coupled to a sCMOS sensor (PCO edge 5.5), mounted with a 10 µm thick GGG_{Eu} scintillator. Scans were performed using single propagation distance

tomography (15 mm sample-to-detector propagation distance), an exposure time of 250-300 ms, 2499 angular projections over a 360⁰ scan, and at voxel sizes of 280, 347 and 700 nm.

Subsequently, 117 additional *Kuehneotherium* specimens (116 isolated teeth and one dentary) and 12 additional *Morganucodon* dentary specimens were scanned during a three-day experiment at the TOMCAT tomographic beamline of the Swiss light Source (SLS), Villigen, Switzerland (13/04/2015-16/04/2015). The beam was set at an energy of 20 keV using a double multilayer monochromator, a LSO:Tb scintillator and a pco.EDGE 5.5 detector. Samples were scanned using single propagation distance tomography (14 mm sample-to-detector propagation distance), an exposure time of 150 ms and 1500 angular projections over a 180⁰ scan at a voxel size of 330 nm. A *Kuehneotherium* lower molar (UMZC Sy 141) was imaged at 1.2 μm voxel size (with an exposure time of 150 ms and 1500 angular projections over 180⁰) to provide the three-dimensional (3D) volume presented in Fig. 1b.

Three juvenile *Morganucodon* dentary specimens with roots from final deciduous premolars (NHMUK PV M 27312, NHMUK PV M 27474 and NHMUK PV M 27475), and an older individual with extensive molar wear (NHMUK PV M 27465), were scanned during a three-day experiment at the TOMCAT beamline of the SLS (07/03/2016-10/03/2016). The beam energy was set at 21 keV using a double multi-layer monochromator. Samples were scanned using single propagation distance tomography (14 mm sample-to-detector propagation distance), an exposure time of 200 ms and 1601 angular projections over a 180⁰ scan at a voxel size of 330 nm.

CT reconstructions of the above tomographic data were generated using a filtered back-projection algorithm coupled with 'Paganin-style' single distance phase retrieval[58] algorithms developed in-house at the respective beamlines[59]. For data from ID19, $\beta = 8.1 \ 10^{-8}$, $\delta = 9.8*10^{-9}$. For data from TOMCAT, $\beta = 3.7 \ 10^{-8}$, $\delta = 1.7 \ 10^{-10}$.

Of the 71 *Morganucodon* specimens imaged at beamline ID19 in 2014, four were additionally imaged at the nano-imaging beamline ID16A of the ESRF synchrotron (project ES 152). These were imaged using holotomography[60] from four propagation distances. Holograms were recorded using a CCD detector with an effective pixel size of 3 um and a 23 μm thick GGG:Eu scintillator at both 17 keV and 33.6 keV. The selected voxel sizes were 10 nm, 25 nm, 30 nm and 130 nm. The number of angular projections recorded over 180^0 varied between 1200 and 2000 and the exposure times were set at 250 to 800 ms. To generate the image containing the virtual section in Figure 1g with 30 nm voxel size, the four focus-to-sample distances were 2.65 mm, 13.19 mm, 15.36 mm and 19.87 mm and the sample-to-detector distance was 1.2648 m.

To produce the 3D model presented in Fig. 1a, a *Morganucodon* lower molar (NHMUK PV M 104134) was imaged using micro CT (μCT) at the University of Helsinki in March 2013. μCT was performed using a Nanotom 180 NF (phoenix|X-ray Systems & Services GmbH) with a CMOS detector (Hamamatsu Photonics) and a high-power transmission-type X-ray nanofocus source with a tungsten anode. A total of 900 angular projections were collected for a 180° rotation, at an exposure time of 1840 ms and a voxel size of $2*2*2$ μm³. The raw projection data were reconstructed using filtered back-projection by the reconstruction software datos|x rec, supplied by the system manufacturer.

Increment counting and the creation of virtual thin sections

Cementum increments were counted in CT data using modifications to the techniques suggested by the Cementochronology Research Program[38] to take into account the 3D nature of the PPC-SRμCT cementum data. First, the cementum was visually inspected throughout the entire volume of each scan, in transverse PPC-SRμCT slices using ImageJ/Fiji[61] to distinguish between specimens that could be confidently interpreted as preserving cementum

increments, and those that were too badly affected by diagenesis for increment counting. Phase contrast imaging of incremental features is understood to be prone to recurrent destructive interference patterns from Fresnel diffraction that create periodic blurring at differing frequencies when they are scanned using inappropriate experimental parameters (principally X-ray energy, sample-to-detector propagation distance and voxel size). However, our parameters produce blurring frequencies that are too narrow (approx. 500-900 nm) to significantly affect the contrast between cementum increments (1-3 μm radial thickness) (Tafforeau *Pers. Obs.*). Therefore, no significant masking of increments from Fresnel diffraction blurring should be expected in our data. In specimens that preserved increments, volumes were inspected by eye to identify regions of highest increment contrast with no lensing and/or coalescence between increments. Increments identified in these regions were followed by eye throughout the entire cementum tissue surrounding these regions, both longitudinally and transversely through the root, in order to distinguish between principal increments and accessory increments formed by lensing and coalescence of primary increments in discrete portions of the tissue (SI Fig. 1). Primary increments were distinguished as those that persisted vertically through the entire scanned region of cementum, whereas accessory increments lasted only for short periods before coalescing into neighbouring increments (SI Fig. 1).

Once regions of highly contrasting primary cementum increments had been identified, virtual thin sections of these regions were created. This was performed by isolating 10 transverse PPC-SRμCT slices through each region and summing their greyscale values using the "Sum slices" option of the "Z projection" tool in ImageJ/Fiji to create a new image of increased contrast between dark and light cementum increments and reduced image noise. Between three and five virtual thin sections were created for all specimens with readable cementum increments. For each virtual thin section, increments were counted manually by

three different observers: Observer One (EN) had considerable experience in counting

cementum increments (>100 specimens studied); Observer Two (KW) had training in

counting cementum increments (30 specimens studied under guidance from Observer One)

and experience in studying growth patterns in PPC-SRμCT data of long-bones; Observer

Three (CN) had no prior experience in counting increments or studying growth patterns. Each

observer studied virtual thin sections blind, after collections of virtual thin sections were

numbered and randomized between specimens using the RAND function in Microsoft Excel.

For each observer, the final increment count for every specimen was determined as the

maximum number counted in all of its virtual thin sections.

Once each observer had counted increments in every virtual thin section (SI Fig. 3)

(SI Table 1), the precision between their increment counts was compared by calculating the

coefficient of variation (*CV*; formula 1) (SI Table 3):

1. $$CV = \left[\frac{standard\ deviation}{mean}\right] * 100$$

3D modelling of cementum increments

3D modelling was performed, using Avizo image analysis software (Avizo 8.0; Thermo

Fisher Scientific), on a subsample of teeth comprising the first tooth imaged using PPC-

SRμCT (NHMUK PV M 104131), and the specimens that provided the highest cementum

increment counts for each fossil taxon (NHMUK M 104127 for *Morganucodon* and UMCZ

Sy 141 for *Kuehneotherium*). Original tomographic data was downsampled in each axis by a

factor of two to decrease manual processing time while retaining sufficient spatial resolution

to preserve the cementum increments. Principal increments originally identified by eye were

manually traced in each PPC-SRμCT slice and assigned to different materials in the 'label

field' tool-kit. Models were subsequently created and analysed using the 'surface view'

feature of Avizo. This allowed the pattern of incrementation to be viewed with a 3D

perspective, to test whether increments defined in two-dimensional slices were true principal increments or diffuse accessory increments (SI Fig. 1).

Body mass estimation for *Morganucodon* and *Kuehneotherium* and choice of extant taxa for physiological comparison

The body masses of our fossil taxa were estimated using two techniques, based on scaling between single cranial dimensions and measured body mass in extant mammals. Maximum body mass estimates were made using the scaling relationship between dentary length (mm) and body mass (g) published for extant marsupial mammals of small body mass, and subsequently used to estimate body mass in several Mesozoic fossil taxa from the Late Jurassic Morrison Formation and elsewhere[45]:

2.   ln body mass(g) = 2.9677*(ln dentary length(mm)) – 5.6712

Dentary lengths are from published CT reconstructions[1] (20 mm for *Morganucodon* and 21.9 mm for *Kuehneotherium*), resulting in body mass estimates of 25.0 g and 32.7 g respectively. However, this estimate may be an overestimate for *Kuehneotherium* as it has a longer, more gracile dentary relative to *Morganucodon*, due to the differing feeding ecologies of the two taxa[1]

Secondly, minimum body mass estimates were calculated using the scaling relationship between skull length (mm) and body mass (g) found for 64 extant species of small 'lipotyphlan' insectivores[62] and used to estimate the body masses of several Mesozoic mammaliaforms[21,62,63].

3.   Ln(body mass(g)) = 3.68*(ln(skull length(mm)) – 3.83

Due to a lack of complete, diagnostic cranial material for UK samples of *Morganucodon* and *Kuehneotherium*, their skull lengths were estimated using a scaling relationship between dentary length and skull length calculated for *Morganucodon oehleri* from Rowe et al. Figure S1[21] (skull length(mm) = 1.0458*jaw length(mm)). Following this relationship, we used dentary length[1,21] to estimate a skull length of 21.0 mm for *Morganucodon watsoni* and 22.9 mm for *Kuehneotherium*, which results in body mass estimates of 10.7 g and 14.9 g respectively (as above this may be an overestimate for *Kuehneotherium*). Body masses presented in Figures 5,7 are mean values of the two estimates (17.9 g for *Morganucodon* and 23.8 g for *Kuehneotherium*).

Extant data

Information on maximum wild lifespan and mean body mass was obtained for 278 extant terrestrial mammal species (body mass: mean = 70.2 kg, standard deviation = 395 kg; wild lifespan: mean = 10.8 years, standard deviation = 11.2 years) and 256 extant terrestrial non-avian reptile species (body mass: mean = 3.6 kg, standard deviation = 20 kg; wild lifespan: mean = 12 years, standard deviation = 14 years) (SI Table 5). Information on maximum captive lifespan was obtained for 644 extant terrestrial mammal species (body mass: mean = 62.2 kg, standard deviation = 324 kg; captive lifespan: mean = 15.5 years, standard deviation = 11.5 years) and 866 extant reptile species (body mass: mean = 2.4 kg, standard deviation = 15.9 kg; captive lifespan: mean = 15.3 years, standard deviation = 11.6 years). Information for flying or gliding taxa (including birds) was not included as their body masses are known to be secondarily reduced to aid their lifestyle and so may distort observed overall relationships between lifespan and body mass[63-65]. In particular, birds and bats live on average three-to-four times as long as terrestrial mammals of similar body mass[66]. Marine

mammals were not included as their environment positively affects their available body mass, allowing significantly higher body masses than terrestrial taxa[67-70]. Mammal wild and captive lifespan data was obtained from the primary literature. The majority of these data originated from a download from the online databases of the Max Planck Institute (https://www.demogr.mpg.de/longevityrecords/0203.htm) on 10/03/2019. The majority of reptile wild and captive lifespans were obtained from the supplementary information of Scharf et al.[71]. Body mass estimates were obtained from an online *Ecological Archives* database[72] (http://www.esapubs.org/archive/ecol/E084/094/metadata.htm), the AnAge database (https://genomics.senescence.info/species/), and published data[50,71]. Although the Max Planck Institute data is entitled "longevity records", it notes in the introduction that this is equivalent to "highest documented age". The authors of the database believe that despite any analytical and conceptual shortcomings, the records are useful in a number of comparative and disciplinary contexts, including demographic, gerontological, ecological and evolutionary. Similarly, the AnAge database states that maximum longevity is synonymous with maximum lifespan.

Data on standard metabolic rate (SMR) for extant mammals (n=117; mean = 915; standard deviation = 3018) and reptiles (n=55; mean = 62.3; standard deviation = 159) was obtained from a published electronic appendix[50]. SMRs for mammals were included in this dataset only if measured under basal metabolic conditions[50] and so are synonymous with basal metabolic rates.

Data on the post-natal growth rate constant *K* was obtained upon request for extant mammals[32] (n = 115, mean = 0.03, standard deviation = 0.03), and reptiles (n=33, mean = 0.002, standard deviation = 0.003) from previous publications[73,74]. The growth rate constant *K* is a magnitude free measure of growth rate, measured in days^{-1}, that is considered the best measure for comparing growth rates between multiple species[75].

Physiological metrics (lifespan/body mass/SMR/K) were compared using phylogenetic generalised least squares (PGLS) regression in the "R" statistical environment with the "ape", "geiger", "nlme" and "phytools" packages installed. For each regression, phylogenetic subsets of squamate and mammal taxa were downloaded from https://vertlife.org (100 trees per subset, birth-death node-dated completed tree distribution for mammals) representing the phylogenetic relationships of every taxon in the respective subsample. For crocodilian taxa, a phylogeny was manually constructed in R following the time-calibrated phylogeny of Oaks[76] (using node mean age values from the species tree/90My maximum analysis) and added to the base of the squamate phylogeny to produce a reptile clade. Each subset was investigated to find the tree that produced the highest PGLS F values and this tree was then input into the "corPagel" covariance structure for the "gls()" function to produce a phylogenetically informed regression model between the respective metrics.

The relationships between body mass and maximum lifespan were compared between extant mammals and extant reptiles using phylogenetic ANCOVA following Smaers et al.[77] using the "gls.ancova" function in "R" with the same libraries installed as for PGLS. The individual phylogenetic subsets representing the mammal and reptile samples were combined with connecting branches connecting the Last Common Ancestors (LCAs) of the crocodilian, squamate and mammal clades. The LCA node connecting squamates and crocodilians was dated at 275.9 Ma using the mean of minimum and maximum node ages from Benton *et al.*[78]; similarly, the LCA node connecting reptiles (squamates and crocodiles) and mammals was dated at 325.5 Ma[78]. The mammal and reptile clades were then distinguished using two factor elements, and the influence of these factors upon the fit of the data to a series of models of increasing complexity was tested. Firstly, a baseline model was produced consisting of one slope and one intercept for the entire dataset. Three models were then compared to this

baseline; the first varied in slope between mammals/reptiles, keeping their intercepts constant; the second allowed the intercept to vary between mammals/reptiles, keeping their slopes constant; and the final model allowed both slope and intercept to vary between mammals/reptiles. Comparisons between these models allowed the determination of their improvements upon the baseline model. Phylogenetic ANCOVA identified a lambda value of <0.001 between body mass and Q_i for reptiles and mammals, and so non-phylogenetically informed GLS and ANCOVA were used to compare these metrics.

μCT study of femoral nutrient foramina

Nutrient foramina in the femora of *Morganucodon* and 11 extant mammal taxa of comparable size were imaged using μCT in the X-Ray Micro-Imaging Laboratory, University of Helsinki (SI Table 4). We used μCT data of femoral foramina rather than photographic images of the foramina[51] because many of the *Morganucodon* foramina were filled with sediment, making their photographic measurement difficult or impossible, whereas the differential density of sediment and fossilized bone in μCT data allowed visualization and analysis. Six *Morganucodon* femur specimens were selected for analysis from the collections of the Cambridge University Museum of Zoology based on their relative completeness. All femora (both fossil and extant) were scanned using a Bruker Skyscan 1272 μCT scanner at 70 kVp source tension and with a 0.5mm Al filter. For each scan, 1125 to 1800 angular projections were collected during a 180⁰ rotation, at an exposure time of 1344 ms. One fossil specimen was scanned at an isotropic voxel size of 4 μm (Fig. 7a), and five at 5 μm. All femora from extant taxa were scanned at 4μm voxel sizes. The raw projection data were reconstructed using filtered back-projection with the Feldkamp algorithm by the Bruker reconstruction software "NRecon" (Version 1.7.1.0).

Analysis of μCT femora data was conducted using Avizo image analysis software (Version 9.3.0; Thermo Fisher Scientific). Foramina were located using the "Orthoslice" tool, to scroll through transverse CT slices of each femur. Once located, the foramen was imaged in 3D using the "Volume rendering" tool. This allowed the minimum diameter, and so minimum radius (in cm), of the foramen aperture to be assessed and measured using the "3D line measurement" tool. Minimum diameter was used by Seymour et al.[51], in the study of foramina in small mammals, as it is not always possible to see the direction of nutrient vessel penetration. Resulting foramina radii were used to generate estimates of blood flow index (Q_i) following the method outlined in Seymour et al.[51]. If multiple foramina were found in a single specimen, then the radii were summed following the assumption that this represents the total entry/exit potential of nutrient circulation through the femur[51]. This sum radius, or the single radius in specimens with single foramina (both abbreviated to r; measured in cm), was then used along with the length of the femur (L; measured in cm) to estimate Q_i as follows:

4. $$Q_i = r^4/L$$

Although *Morganucodon* femoral elements are relatively common in the *Hirmeriella* fissure suite, almost all are incomplete[79]. We here chose the six most complete femoral specimens known from the Pontalun 3 fissure from where the *Morganucodon* teeth imaged using PPC-SRμCT originated. Specimens chosen (UMZC EoPC 19_1 to EoPC 19_6) preserve at least two thirds of the femoral shaft. Length was estimated from the minimum mid-shaft diaphysial width of each element, using the scaling relationship between the two measurements established for a reconstructed *Morganucodon* femur created by concatenating three incomplete femora by PGG:

5.   Femur length = 10.3 * maximum mid-diaphysial diameter

Statistics. One-way ANOVA comparison of intra-observer CV between cementochronological studies; Shapiro-Wilks normality test: PPC-SRμCT data $W = 1$, $p = 1$, histological data $W = 0.93$, $p = 0.41$; test statistics F = 11.12, degrees of freedom(df) = 10, Cohen's effect size $d = 3.13$, $p = 0.00728$. Phylogenetic ANCOVA comparison of PGLS regression slopes for lifespan against body mass in mammals ($\log_{10}$ lifespan = 0.26($\log_{10}$ body mass) + 0.16; 95% CI = 0.05; $r^2 = 0.69$) and reptiles ($\log_{10}$ lifespan = 0.26($\log_{10}$ body mass) + 0.60; 95% CI = 0.08); $r^2 = 0.46$); slopes are statistically similar ($F = 0.868$, $p = 0.352$) while means are significantly separated ($F = 4.44$, df = 529, partial eta squared effect size = 0.32, $p = 0.036$). PGLS regression of mammalian lifespan against msSMR: $\log_{10}$ msSMR = -0.237($\log_{10}$ lifespan) – 0.083; 95% CI = 0.07; $r^2 = 0.59$, $p < 0.001$. PGLS regression of reptilian lifespan against msSMR: $\log_{10}$ msSMR = -0.83($\log_{10}$ lifespan) – 0.31; 95% CI = 0.255; $r^2 = 0.43$, $p < 0.01$. PGLS regression of mammalian lifespan against growth constant K; $\log_{10} K$ = -0.692($\log_{10}$ lifespan) – 1.171; 95% CI = 0.101; $r^2 = 0.66$, $p < 0.01$. PGLS regression of reptilian lifespan against growth constant K; $\log_{10} K$ = -0.69($\log_{10}$ lifespan) – 2.523; 95% CI = 0.339; $r^2 = 0.43$, $p < 0.01$. One-way ANCOVA comparison of OLS regression slopes for Q_i against body mass in extant mammals ($\log_{10}(Qi) = 0.513*\log_{10}$(body mass) - 6.104) and non-varanid reptiles ($\log_{10}(Qi) = 0.685*\log_{10}$(body mass) - 8.139); slopes are statistically similar ($F = 2$, $p = 0.16$) while means are significantly different ($F = 87.6$, df = 89, partial eta squared effect size = 0.50, $p = 7.4E^{-15}$).
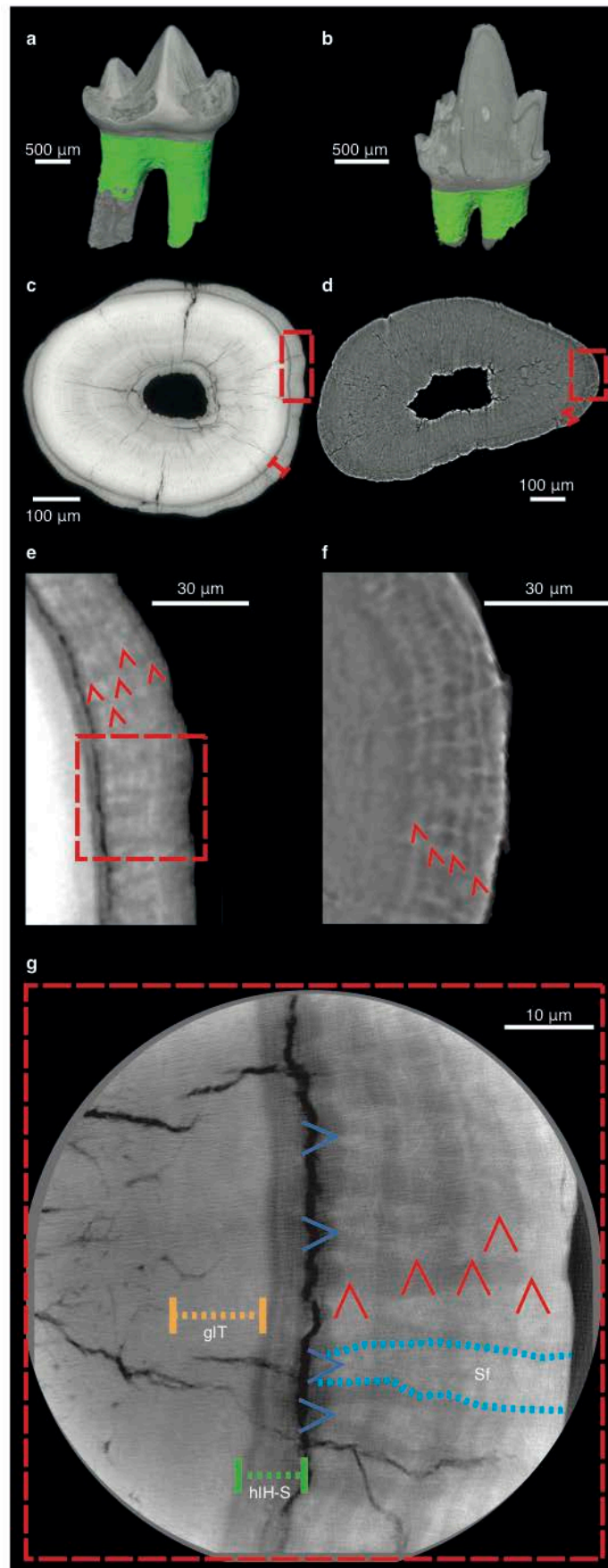
Figure 1

Figure 1 | Cementum of *Morganucodon* and *Kuehneotherium*. a, **b** Three-dimensional reconstructions of **a**, *Morganucodon* right lower molar tooth NHMUK PV M 104134 (voxel size 2 μm, μCT) and **b**, *Kuehneotherium* right lower molar tooth NHMUK PV M 21095 (voxel size 1.2 μm, PPC-SRμCT). Green = cementum. **c**, **d** Transverse PPC-SRμCT virtual thin sections (0.33 μm voxel size) of roots of **c**, NHMUK PV M 104134 and **d**, NHMUK M 27436. Red bracketed line highlights extent of cementum surrounding dentine. **e**, **f** Close-ups of boxes in **c**, **d**, with five and four circumferential light/dark increment pairs highlighted by red arrows, respectively. **g**, Synchrotron nanotomographic virtual thin section of NHMUK PV M 104134 (30 nm voxel size) provides close-up of region close to box in **e.** Vertical red arrows = cementum increments; horizontal blue arrows, dashed blue lines and Sf = radial bands of Sharpey's fibres; yellow dashed line and glT = granular layer of Tomes; green dashed line and hlH-S = hyaline layer of Hopewell-Smith.
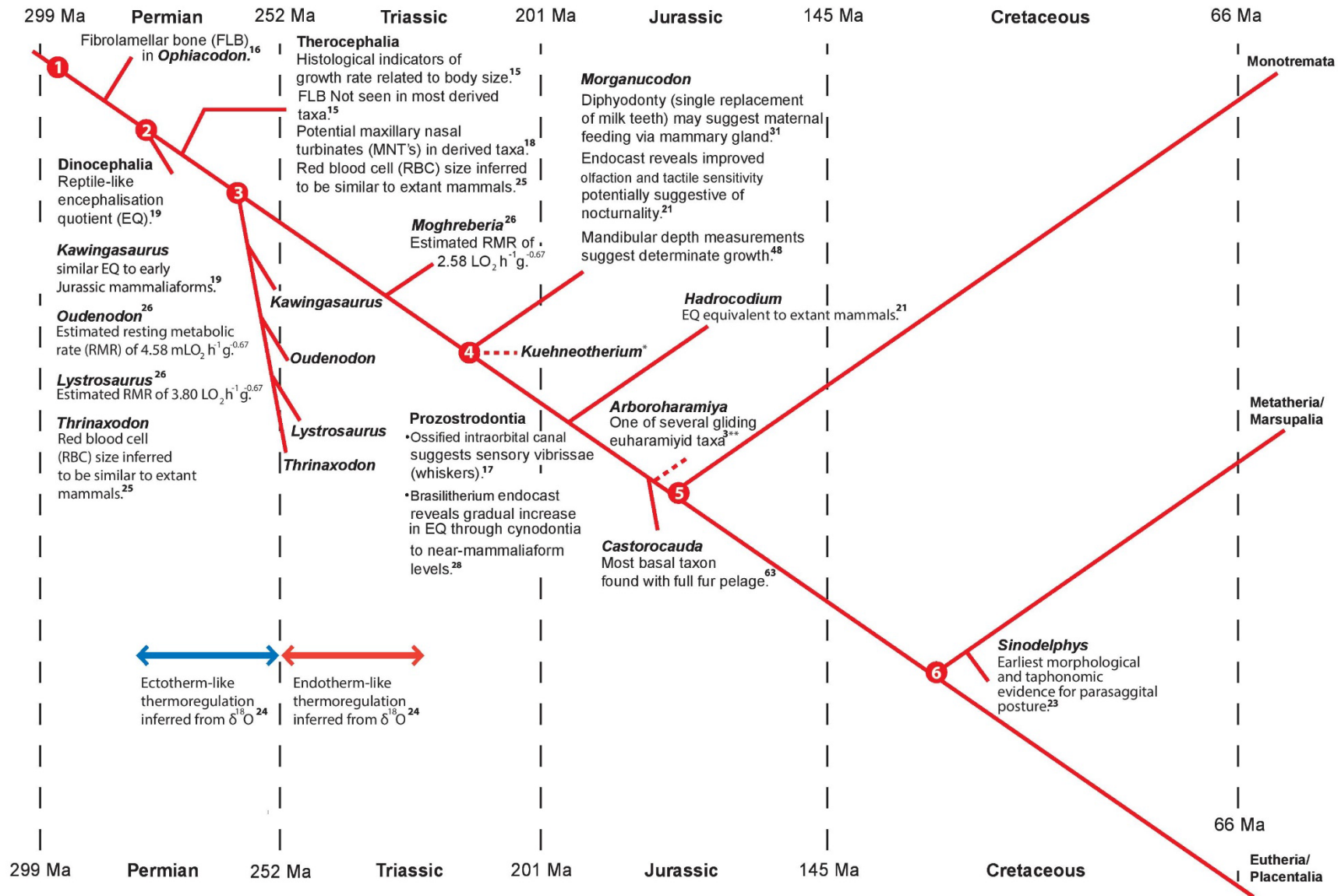
Figure 2

Monotremata

1

Fibrolamellar bone (FLB) in *Ophiacodon*.[16]

Therocephalia
Histological indicators of growth rate related to body size.[15]
FLB Not seen in most derived taxa.[15]
Potential maxillary nasal turbinates (MNT's) in derived taxa.[18]
Red blood cell (RBC) size inferred to be similar to extant mammals.[25]

Morganucodon
Diphyodonty (single replacement of milk teeth) may suggest maternal feeding via mammary gland.[31]
Endocast reveals improved olfaction and tactile sensitivity potentially suggestive of nocturnality.[21]
Mandibular depth measurements suggest determinate growth.[48]

2

Dinocephalia
Reptile-like encephalisation quotient (EQ).[19]

3

Kawingasaurus
similar EQ to early Jurassic mammaliaforms.[19]

Oudenodon[26]
Estimated resting metabolic rate (RMR) of 4.58 mLO$_2$ h^{-1}g$^{0.67}$.

Lystrosaurus[26]
Estimated RMR of 3.80 LO$_2$ h^{-1}g$^{-0.67}$.

Thrinaxodon
Red blood cell (RBC) size inferred to be similar to extant mammals.[25]

Moghreberia[26]
Estimated RMR of 2.58 LO$_2$ h^{-1}g$^{-0.67}$.

Kawingasaurus

Oudenodon

Lystrosaurus

Thrinaxodon

4 - - - *Kuehneotherium**

Hadrocodium
EQ equivalent to extant mammals.[21]

Prozostrodontia
• Ossified intraorbital canal suggests sensory vibrissae (whiskers).[17]
• Brasilitherium endocast reveals gradual increase in EQ through cynodontia to near-mammaliaform levels.[28]

Arboroharamiya
One of several gliding euharamiyid taxa[3**]

Castorocauda
Most basal taxon found with full fur pelage.[63]

5

6

Sinodelphys
Earliest morphological and taphonomic evidence for parasaggital posture.[23]

Metatheria/ Marsupialia

Ectotherm-like thermoregulation inferred from δ^{18}O[24]

Endotherm-like thermoregulation inferred from δ^{18}O[24]

66 Ma

Eutheria/ Placentalia

Figure 2 | Time-scaled phylogeny summarising evidence for physiological evolution along the synapsid lineage towards mammals. Red nodes highlight the divergence of major lineages; Node 1 = divergence of the Pelycosaur lineage; Node 2 = the Therapsida clade; Node 3 = the Cynodontia clade; Node 4 = the Mammaliaformes clade; Node 5 = the Mammalia clade; Node 6 = the Theria clade. Superscript numbers denote references in the main text. * Denotes the uncertain phylogenetic affinities of *Kuehneotherium* within the Mammaliaformes clade[31]. ** Denotes the uncertain phylogenetic affinities of *Arboroharamiya*[3].

Figure 3.
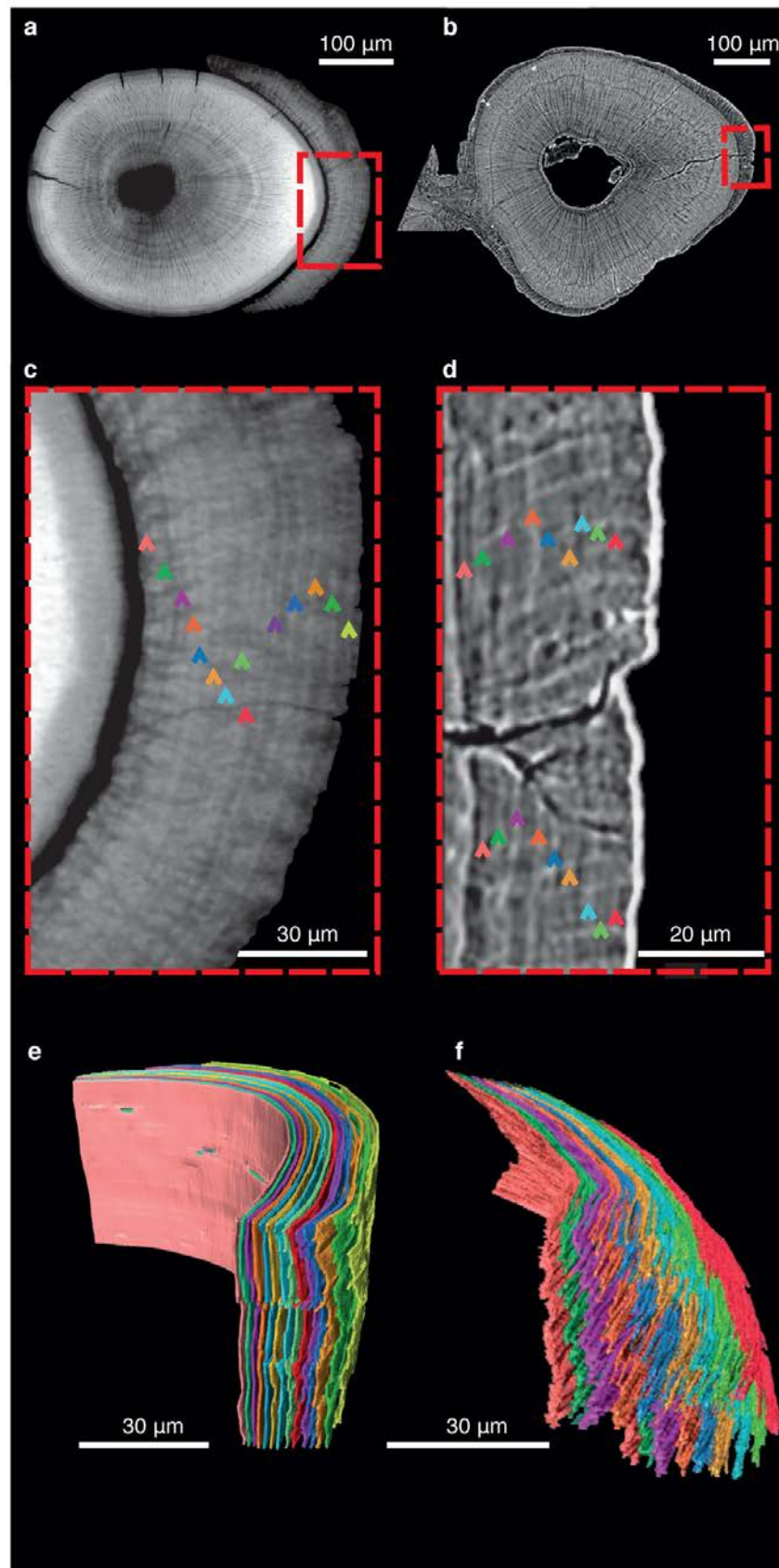
Figure 3 | Three-dimensional segmentation of *Morganucodon* and *Kuehneotherium* specimens with the highest counts of cementum increments. a, **b** Transverse virtual thin-sections of PPC-SRµCT reconstructions (0.33 µm^3 voxel size). **a**, *Morganucodon* specimen NHMUK PV M 104127 showing a 55 µm thick layer of cementum around the root dentine. **b**, *Kuehneotherium* specimen UMZC Sy 141 showing a 32 µm thick layer of cementum. **c**, **d** Detail of the cementum of **c**, NHMUK PV M 104127 and **d**, UMZC Sy 141. Cementum increments highlighted by 14 and nine multi-coloured arrows, respectively. **e**, **f** 3D segmentations of the cementum increments of **e**, NHMUK PV M 104127, and **f**, UMZC Sy 141. The colour of each increment corresponds to the colours of each arrow in **c** and **d** respectively.

Figure 4
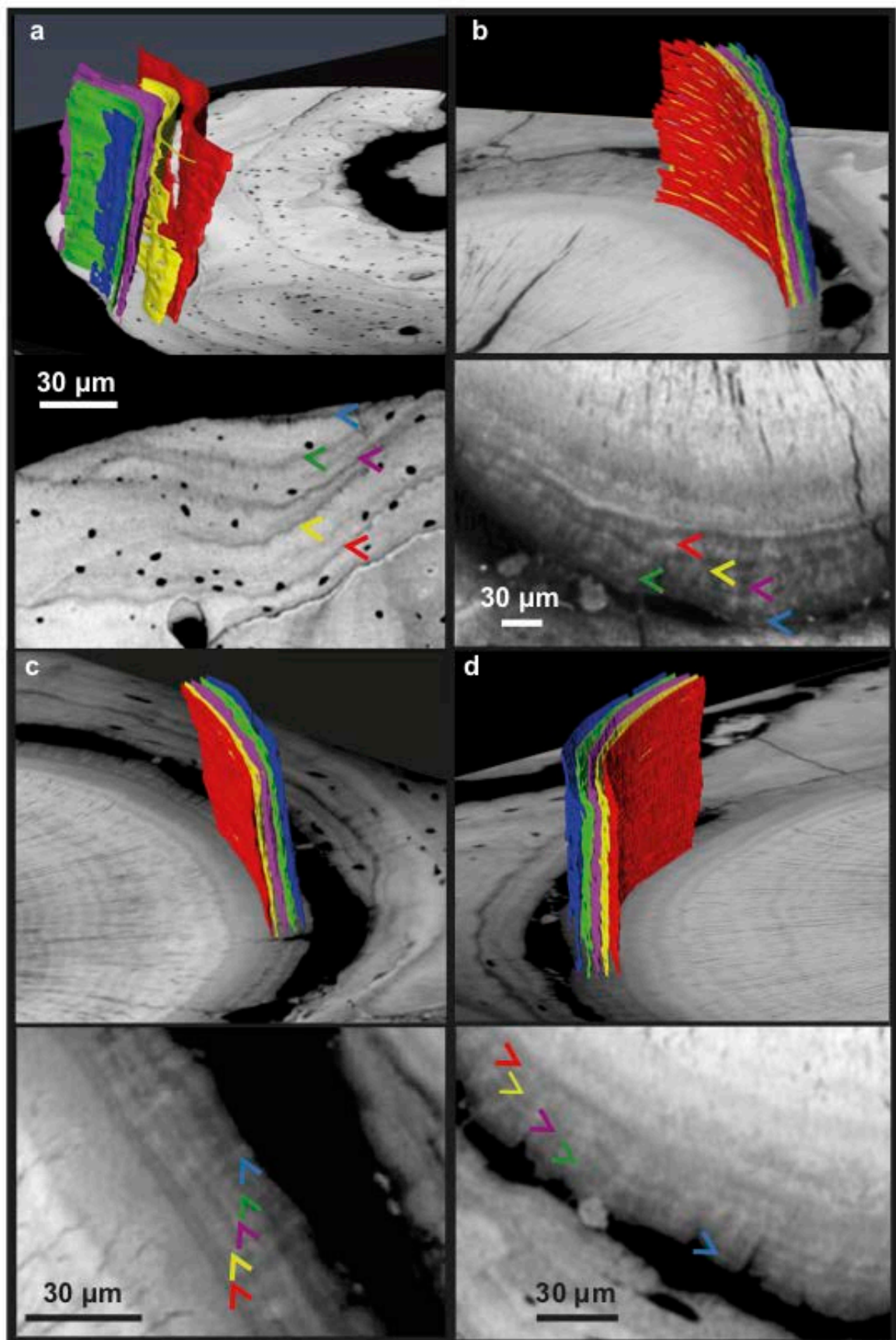
Figure 4 | Shared increment patterns between m1 and m2 tooth-root cementum and the dentary of *Morganucodon* specimen NHMUK PV M 96413. a, Four lines of arrested growth and a fifth incipient one are visible within the periosteal region of the dentary, each highlighted by three-dimensional segmented bands of differing colour corresponding to coloured arrows in the accompanying transverse PPC-SRμCT slice. Only LAGs persisting through the volume are segmented and highlighted. This pattern is mirrored in **b,** the anterior root of the m1 tooth; **c,** the posterior root of the same m1 tooth; and **d,** the anterior root of the m2 tooth.

Figure 5
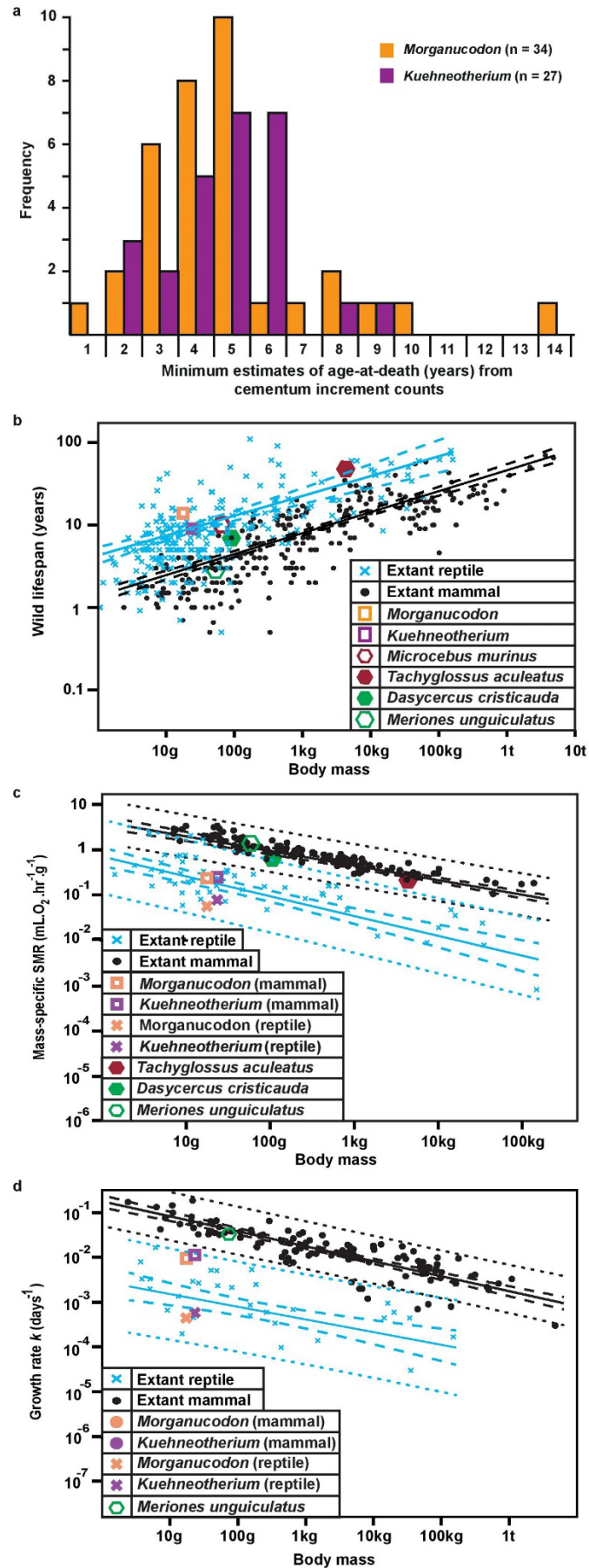
Figure 5 | Lifespan and metabolic estimates of *Morganucodon* and *Kuehneotherium*. a, Histogram of lifespan estimates from cementum increment counts. **b**, Log_{10} phylogenetic least squares (PGLS) biplot of mean body mass (g) against maximum wild lifespan (years) for extant mammals (n = 279), extant non-avian reptiles (n = 252), and fossil mammaliaforms. **c,** Log_{10} PGLS biplot of mean body mass (g) against mass specific standard metabolic rate (msSMR; $mL.O_2.hr^{-1}.g^{-1}$) for extant mammals (n = 117) and extant reptiles (n = 55), and estimates for fossil mammaliaforms. **d,** Log_{10} PGLS biplot of mean body mass (g) against post-natal growth rate constant K ($days^{-1}$) for extant mammals (n = 115) and extant reptiles (n = 33) and estimates for fossil mammaliaforms. PGLS regression lines in **b–d** are shown for extant mammals (black) and extant reptiles (blue), 95% confidence intervals are represented by dashed lines, 95% predictor intervals by dotted lines. Source data are provided as a Source Data file.

Figure 6
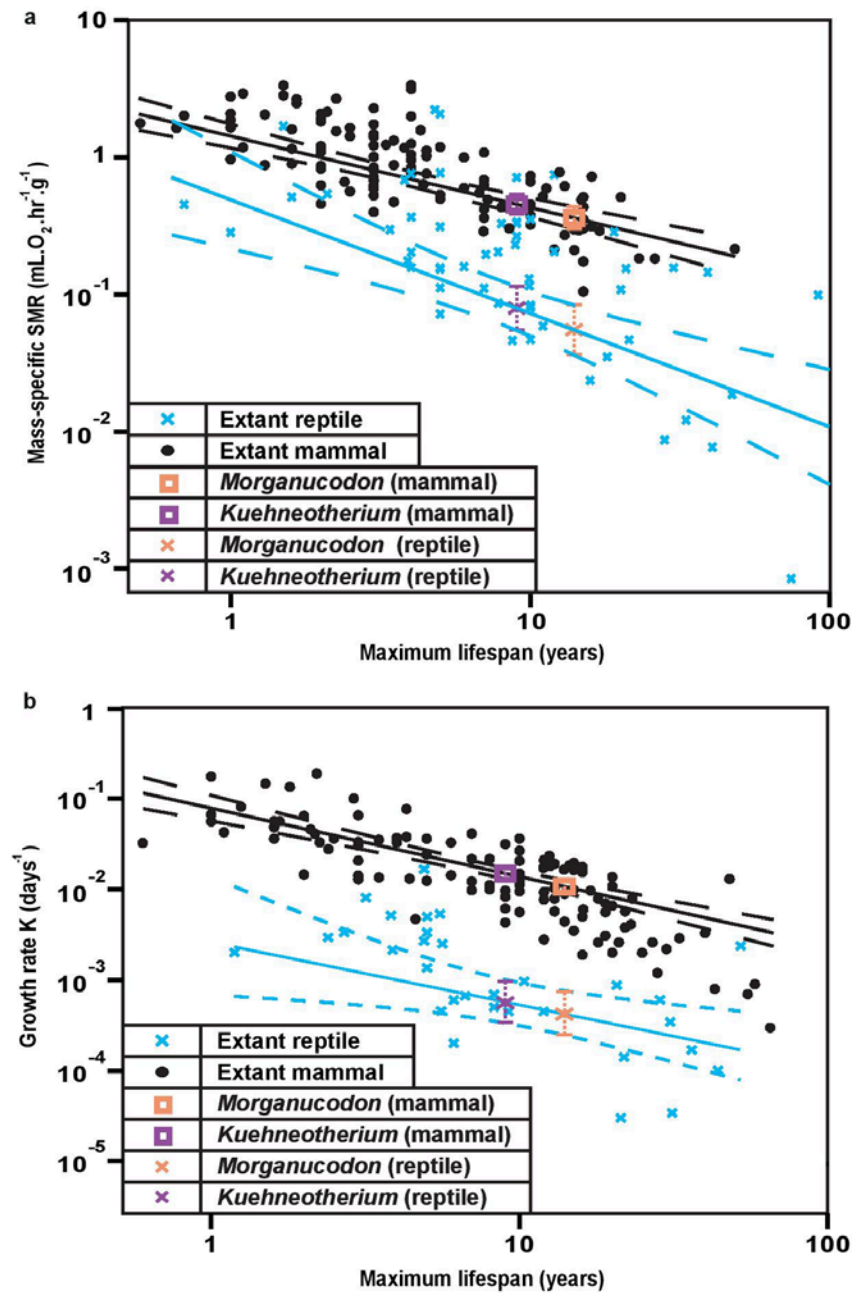
Figure 6 | The relationship between lifespan and msSMR, and lifespan and growth rate constant *K*, in mammals and reptiles. a, Log$_{10}$ phylogenetic least squares (PGLS) biplot between maximum wild lifespan (years) and mass-specific standard metabolic rate (msSMR; mL.O$_2$.hr^{-1}.kg^{1}) for extant mammals (n=117) and reptiles (n=55). **b,** Log$_{10}$ PGLS biplot between maximum wild lifespan (years) and post-natal growth rate constant *K* (days^{-1}) for extant mammals (n=115) and reptiles (n=31). PGLS regression means for each clade (black lines for mammals, blue lines for reptiles, dashed lines denote 95% confidence intervals) are used to estimate msSMR and *K* for mammaliaforms *Morganucodon* and *Kuehneotherium*, with dashed brackets denoting their 95% confidence intervals. Source data are provided as a Source Data file.

Figure 7
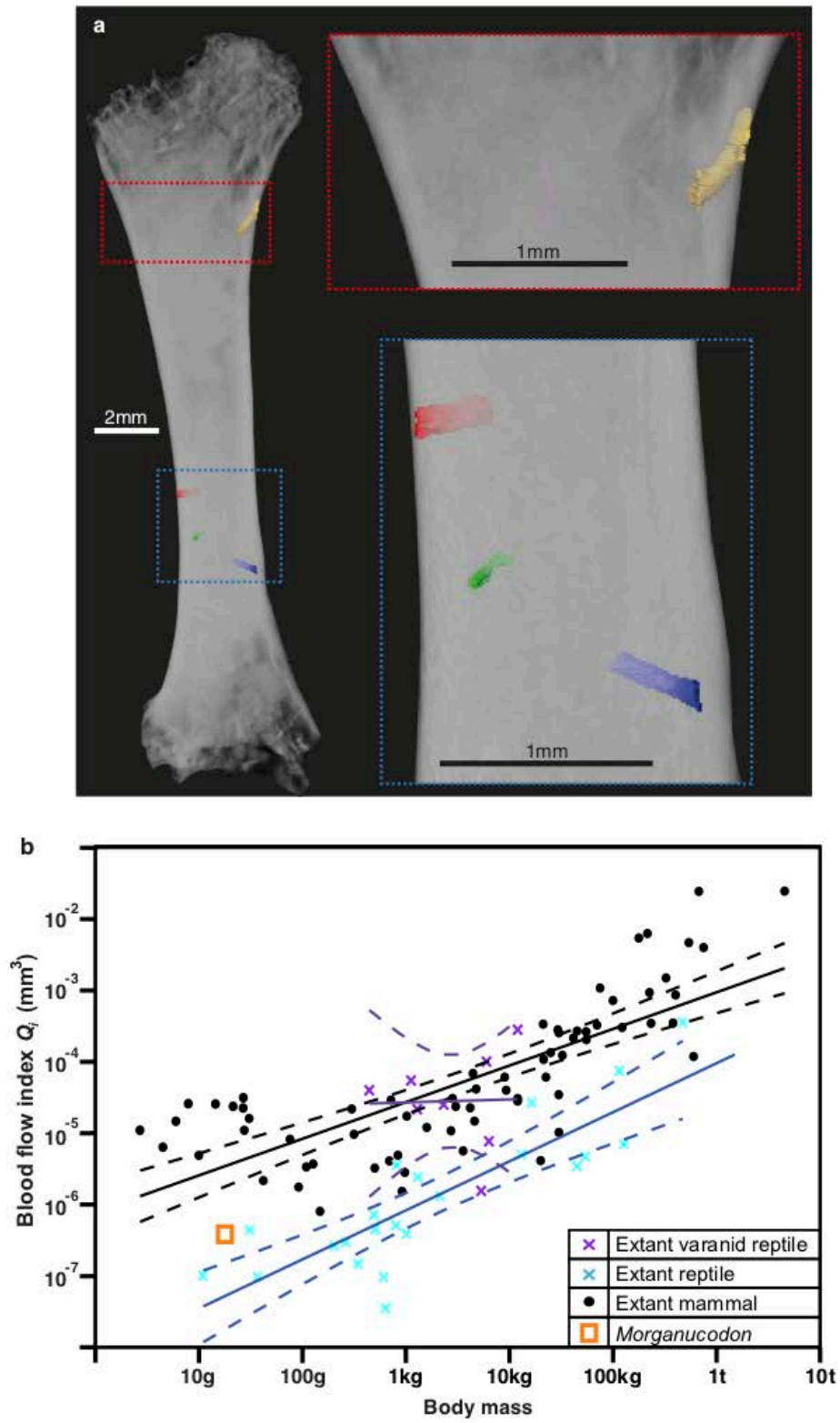
Figure 7 | Femoral foramina and estimates of relative femoral bloodflow for

Morganucodon. **a**, 3D reconstruction of *Morganucodon* femur using μCT (specimen UMZC Eo PC 19_6, voxel size of 4 μm), with all identifiable foramina segmented and highlighted (red, green, gold and blue). **b**, $\log_{10}$ biplot of mean body mass (g) against estimated blood flow index (Qi; mm^3) for extant non-avian reptiles (n = 22), extant varanid reptiles (n=8), extant mammals (n=69), and *Morganucodon*. GLS regression lines in **b** are shown for extant mammals (black), extant non-varanid reptiles (blue) and extant varanids (purple), with 95% confidence intervals represented by dashed lines. Source data are provided as a Source Data file.

Table 1

Specimen	Element	Increments
NHMUK PV M 95790	i4	7
NHMUK PV M 95790	c	7
NHMUK PV M 95790	p1	8
NHMUK PV M 95790	p2	8
NHMUK PV M 95790	p3	8
NHMUK PV M 96413	p3	5
NHMUK PV M 96413	p4	5
NHMUK PV M 96413	m1	5
NHMUK PV M 96413	dentary	5
NHMUK PV M 96396	p4	4
NHMUK PV M 96396	m1	4
NHMUK PV M 96396	m2	4
NHMUK PV M 96396	m3	3
NHMUK PV M 96396	dentary	4
NHMUK PV M 95809	m1	3
NHMUK PV M 95809	m2	3
NHMUK PV M 104128	m1	5
NHMUK PV M 104128	m2	5
NHMUK PV M 96441	m1	5
NHMUK PV M 96441	m2	5
NHMUK PV M 104130	m1	5
NHMUK PV M 104130	m2	5
NHMUK PV M 104130	m3	4
NHMUK PV M 104129	m1	9
NHMUK PV M 104129	m2	9
NHMUK PV M 104129	m3	8

Table 1 | Cementum and dentary increment counts for each element of dentulous *Morganucodon* specimens. The lower dental formula of *Morganucodon* is 4:1:4:4-5[1].

Data Availability

The tomographic data that support the findings of this study are available from the corresponding authors upon reasonable request. The source data underlying figs 5, 6, and 7 and S3, S4, and S5 are provided as a Source Data file.

References

1. Gill, P. G., Purnell, M. A., Crumpton, N., Brown, K. R., Gostling, N. J. et al. Dietary specializations and diversity in feeding ecology of the earliest stem mammals. *Nature* **512**, 303–305 (2014).

2. Luo, Z. X. Transformation and diversification in early mammal evolution. *Nature* **450**, 1011–1019 (2007).

3. Han, G., Mao, F., Bi, S., Wang, Y., & Meng, J. A Jurassic gliding euharamiyidan mammal with an ear of five auditory bones. *Nature* **551**, 451–456 (2017).

4. Wilson, G. P., Evans, A. R., Corfe, I. J., Smits, P. D., Fortelius, M. et al. Adaptive radiation of multituberculate mammals before the extinction of dinosaurs. *Nature* **483**, 457–460 (2012).

5. Close, R. A., Friedman, M., Lloyd, G. T., & Benson, R. B. Evidence for a mid–Jurassic adaptive radiation in mammals. *Curr. Biol.* **25**, 2137–2142 (2015).

6. Bennett, A. F., & Ruben, J. A. Endothermy and activity in vertebrates. *Science* **206**, 649–654 (1979).

7. Kemp, T. S. The origin of mammalian endothermy: a paradigm for the evolution of complex biological structure. *Zool. J. Linn. Soc.* **147**, 473–488 (2006).

8. Clarke, A., & Pörtner, H. O. Temperature, metabolic power and the evolution of endothermy. *Biol. Rev.* **85**, 703–727 (2010).

9. Koteja, P. Energy assimilation, parental care and the evolution of endothermy. *Proc. Royal Soc. B* **267**, 479–484 (2000).

10. Hopson, J. A. The role of foraging mode in the origin of therapsids: implications for the origin of mammalian endothermy. *Fieldiana Life Earth Sci.* **49**, 126–149 (2012).

11. Farmer, C. G. Reproduction: the adaptive significance of endothermy. *Am. Nat.* **162**, 826–840 (2003).

12. Lovegrove, B. G. The evolution of endothermy in Cenozoic mammals: a plesiomorphic-apomorphic continuum. *Biol. Rev.* **87**, 128–162 (2012).

13. Avaria-Llautureo, J., Hernández, C. E., Rodríguez-Serrano, E., Venditti, C. The decoupled nature of basal metabolic rate and body temperature in endotherm evolution. *Nature* **572**, 651-654 (2019).

14. Gross, W. Die Typen des mikroskopischen Knochenbaues bei fossilen Stegoccphalen und Reptilien. *Anat. and Embryol.* **103**, 731–764 (1934).

15. Ray, S., Botha, J., & Chinsamy, A. Bone histology and growth patterns of some nonmammalian therapsids. *J. Vert. Paleontol.* **24**, 634–648 (2004).

16. Shelton, C. D. & Sander, P. M. Long bone histology of *Ophiacodon* reveals the geologically earliest occurrence of fibrolamellar bone in the mammalian stem lineage. *C. R. Palevol.* **16**, 397–424 (2017).

17. Benoit, J., Manger, P. R., & Rubidge, B. S. Palaeoneurological clues to the evolution of defining mammalian soft tissue traits. *Sci. Rep.* **6**, 25604 (2016).

18. Hillenius, W. J. Turbinates in therapsids: evidence for Late Permian origins of mammalian endothermy. *Evolution* **48**, 207–229 (1994).

19. Benoit, J., Fernandez, V., Manger, P. R., & Rubidge, B. S. Endocranial casts of pre-mammalian therapsids reveal an unexpected neurological diversity at the deep evolutionary root of mammals. *Brain Behav. Evolut*. **90**, 311–333 (2017).

20. Rowe, T. B. Definition, diagnosis, and origin of Mammalia. *J. Vert. Paleontol.* **8**, 241–264 (1988).

21. Rowe, T. B., Macrini, T. E., & Luo, Z. X. Fossil evidence on origin of the mammalian brain. *Science* **332**, 955–957 (2011).

22. Hoffman, E. A., & Rowe, T. B. Jurassic stem–mammal perinates and the origin of mammalian reproduction and growth. *Nature* **561**, 104–108 (2018).

23. Kielan–Jaworowska, Z., & Hurum, J. H. Limb posture in early mammals: sprawling or parasagittal. *Acta Palaeontol. Pol*. **51**, 393–406 (2006).

24. Rey, K., Amiot, R., Fourel, F., Abdala, F., Fluteau, F. et al. Oxygen isotopes suggest elevated thermometabolism within multiple Permo-Triassic therapsid clades. *eLife* **6**, e28589 (2017).

25. Huttenlocker, A. K., & Farmer, C. G. Bone microvasculature tracks red blood cell size diminution in Triassic mammal and dinosaur forerunners. *Curr. Biol*. **27**, 48–54 (2017).

26. Olivier, C., Houssaye, A., Jalil, N. E., & Cubo, J. First palaeohistological inference of resting metabolic rate in an extinct synapsid, *Moghreberia nmachouensis* (Therapsida: Anomodontia). *Biol. J. Linn. Soc*. **121**, 409–419 (2017).

27. Crompton, A. W., Owerkowicz, T., Bhullar, B. A., & Musinsky, C. Structure of the nasal region of non–mammalian cynodonts and mammaliaforms: speculations on the evolution of mammalian endothermy. *J. Vertebrate Paleontol*. **37**, e1269116 (2017).

28. Rodrigues, P. G., Martinelli, A. G., Schultz, C. L., Corfe, I. J., Gill, P. G. et al. Digital cranial endocast of *Riograndia guaibensis* (Late Triassic, Brazil) sheds light on the evolution of the brain in non–mammalian cynodonts. *Hist. Biol*. 1–18 (2018).

29. Hayes, J. P., & Garland Jr, T. The evolution of endothermy: testing the aerobic capacity model. *Evolution* **49**, 836–847 (1995).

30. Köhler, M., Marín–Moratalla, N., Jordana, X., & Aanes, R. Seasonal bone growth and physiology in endotherms shed light on dinosaur physiology. *Nature* **487**, 358–361 (2012).

31. Kielan–Jaworowska, Z., Cifelli, R. L., & Luo, Z. X. *Mammals from the age of dinosaurs: origins, evolution, and structure* (Columbia University Press, New York, United States, 2004).

32. Hulbert, A. J., Pamplona, R., Buffenstein, R., & Buttemer, W. A. Life and death: metabolic rate, membrane composition, and life span of animals. *Physiol. Rev*. **87**, 1175–1213 (2007).

33. Magalhães, J. P. D., Costa, J., & Church, G. M. An analysis of the relationship between metabolism, developmental schedules, and lifespan using phylogenetic independent contrasts. *J. Gerontol. A Biol. Sci. and Med. Sci*. **62**, 149–160 (2007).

34. Werner, J., Sfakianakis, N., Rendall, A. D., & Griebeler, E. M. Energy intake functions and energy budgets of ectotherms and endotherms derived from their ontogenetic growth in body mass and timing of sexual maturation. *J. Theor. Biol.* **444**, 83–92 (2018).

35. Grady, J. M., Enquist, B. J., Dettweiler-Robinson, E., Wright, N. A., & Smith, F. A. Evidence for mesothermy in dinosaurs. *Science* **344**, 1268–1272 (2014).

36. Dong, X., Milholland, B. & Viig, J. Evidence for a limit to human lifespan. *Nature* **538**, 257–259 (2016).

37. Klevezal, G. *Recording structures of mammals*. CRC Press. Boca Raton, Florida, US (1995).

38. Naji, S., Colard, T., Blondiaux, J., Bertrand, B., d'Incau, E. et al. Cementochronology, to cut or not to cut? *Int. J. Paleopathol*. **15**, 113–119 (2016).

39. Lieberman, D. E. Life history variables preserved in dental cementum microstructure. *Science* **261**, 1162–1164 (1993).

40. Stock, S. R., Finney, L. A., Telser, A., Maxey, E., Vogt, S. et al. Cementum structure in Beluga whale teeth. *Acta Biomater*. **48**, 289–299, (2017).

41. Stutz, A. J. Polarizing microscopy identification of chemical diagenesis in archaeological cementum. *J. Archaeol. Sci*. **29**, 1327–1347 (2002).

42. Newham, E. *Exploring the Use of X–ray Tomography for the Quantification of Cementum Growth Patterns Across the Mammal Phylogeny*. PhD thesis, Univ. Southampton (2018).

43. Le Cabec, A., Tang, N. K., Ruano Rubio, V., & Hillson, S. Nondestructive adult age at death estimation: Visualizing cementum annulations in a known age historical human assemblage using synchrotron X-ray microtomography. *Am. J. Phys. Anthropol*. **168**, 25–44 (2019).

44. Wittwer–Backhofen, U., Gampe, J., Vaupel, J. W. Tooth cementum annulation for age estimation: results from a large known-age validation study. *Am. J. Phys. Anthropol*. **123**, 119–129 (2004).

45. Foster, J. R. Preliminary body mass estimates for mammalian genera of the Morrison Formation (Upper Jurassic, North America). *PaleoBios* **28**, 114–122 (2009).

46. Whiteside, D. I., Duffin, C. J., Gill, P. G., Marshall, J. E., & Benton, M. J. The Late Triassic and Early Jurassic fissure faunas from Bristol and South Wales: stratigraphy and setting. *Palaeontol. Pol.* **67**, 257–287 (2016).

47. Luo, Z-X, Kielan-Jaworowska, Z. & Cifelli, R. L. In quest for a phylogeny of Mesozoic mammals. *Acta Palaeontologica Polonica.* **47**, 1-78 (2002).

48. O'Meara, R. N., & Asher, R. J. The evolution of growth patterns in mammalian versus nonmammalian cynodonts. *Paleobiology* **42**, 439–464 (2016).

49. Yoder, A. D., Campbell, C. R., Blanco, M. B., Dos Reis, M., Ganzhorn, J. U. et al. Geogenetic patterns in mouse lemurs (genus *Microcebus*) reveal the ghosts of Madagascar's forests past. *PNAS* **113**, 8049–8056 (2016).

50. White, C. R., Phillips, N. F., & Seymour, R. S. The scaling and temperature dependence of vertebrate metabolism. *Biol. Letters.* **2**, 125–127 (2005).

51. Seymour, R. S., Smith, S. L., White, C. R., Henderson, D. M., & Schwarz–Wings, D. Blood flow to long bones indicates activity metabolism in mammals, reptiles and dinosaurs. *Proc. Royal Soc. B* **279**, 451–456 (2011).

52. Kemp, T. S. *The origin and evolution of mammals.* Oxford University Press. Oxford, UK (2005).

53. Lautenschlager, S., Gill, P. G., Luo, Z. X., Fagan, M. J., & Rayfield, E. J. (2018). The role of miniaturization in the evolution of the mammalian jaw and middle ear. *Nature* **561**, 533–537 (2018).

54. Botha–Brink, J., Codron, D., Huttenlocker, A. K., Angielczyk, K. D., & Ruta, M. Breeding young as a survival strategy during Earth's greatest mass extinction. *Sci. Rep.* **6**, 24053 (2016).

55. Kermack, K. A., Mussett, F., & Rigney, H. W. The lower jaw of *Morganucodon*. *Zool. J. Linn. Soc.* **53**, 87–175 (1973).

56. Kermack, D. M., Kermack, K. A., & Mussett, F. The Welsh pantothere *Kuehneotherium praecursoris. Zool. J. Linn. Soc.* **47**, 407–423 (1968).

57. Gill, P. G. Kuehneotherium *from the Mesozoic Fissure Fillings of South Wales.* Ph.D. thesis, Univ. Bristol (2004).

58. Paganin, D., Mayo, S. C., Gureyev, T. E., Miller, P. R. & Wilkins, S. W. Simultaneous phase and amplitude extraction from a single defocused image of a homogeneous object. *J. Microscopy.* **206**, 33-40 (2002).

59. Marone, F. & Stampanoni, M. Regridding reconstruction algorithm for real-time tomographic imaging. *J. Synchrotron Radiation.* **19**, 1029-1037 (2012).

60. Mokso, R. & Cloetens, P. Nanoscale zoom tomography with hard x rays using Kirkpatrick-Baez optics. *Appl. Phys. Lett.* **90**, 144104 (2007).

61. Schneider, C. A., Rasband, W. S. & Eliceiri, K. W. NIH Image to ImageJ: 25 years of image analysis. *Nature Methods.* **9**, 671–675 (2001).

62. Luo, Z. X., Crompton, A. W. & Sun, A. L. A new mammaliaform from the Early Jurassic and evolution of mammalian characters. *Science.* **292**, 1535–1540 (2001).

63. Ji, Q., Luo, Z. X., Yuan, C. X. & Tabrum, A. R. A swimming mammaliaform from the Middle Jurassic and ecomorphological diversification of early mammals. *Science.* **311**, 1123–1127 (2006).

64. Mclean, J. A. & Speakman, J. R. Effects of body mass and reproduction on the basal metabolic rate of brown long–eared bats (*Plecotus auratus*). *Physiol. Biochem. Zool.* **73**, 112–121 (2000).

65. Salmon, A. B., Leonard, S., Masamsetti, V., Pierce, A., Podlutsky, A. J., et al. The long lifespan of two bat species is correlated with resistance to protein and enhanced protein homeostasis. *FASAB J.* **23**, 2317–2326 (2009).

66. Becker, N. I., Encarnacao, J. A., Tschapka, M. & Kalko, E. K. V. Energetics and life–history of bats in comparison to small mammals. *Ecol. Res.* **28**, 249–258 (2013).

67. Munshi–South, J. & Wilkinson, G. S. (2010). Bats and birds: exceptional longevity despite high metabolic rates. *Ageing Res. Rev.* **9**, 12–19 (2010).

68. Kasting, N. W., Adderley, S. A., Safford, T. & Hewlett, K. G. Thermoregulation in beluga (*Delphinapterus leucas*) and killer (*Orcinus orca*) whales. *Physiol. Zool.* **62**, 687–701 (1989).

69. Ortiz, R. M., Noren, D. P., Litz, B. & Ortiz, C. L. A new perspective on adiposity in a naturally obese mammal. *Am. J. Physiol.–Endocrinol. Metab.* **281**, E1347–E1351 (2001).

70. Chikina, M., Robinson, J. D. & Clark, N. L. Hundreds of genes experienced convergent shifts in selective pressure in marine mammals. *Mol. Biol. Evol.* **33**, 2182–1292 (2016)

71. Scharf, I., Feldman, A., Novosolov, M., Pincheira-Donoso, D., Das, I. et al. Late bloomers and baby boomers: ecological drivers of lifespan in squamates and the tuatara. *Global Ecol. Biogeog.* **24** 396–405 (2015).

72. Smith, F. A., Lyons, S. K., Ernest, S. K. M., Jones, K. E., Kaufman, D. M., et al. Body mass of late Quaternary mammals. *Ecology.* **84**, 3403 (2003).

73. Werner, J. & Griebeler, E. M. Allometries of maximum growth rate versus body mass at maximum growth indicate that non–avian dinosaurs had growth rates typical of fast growing ectothermic sauropsids. *PLOS One.* **9**, e88834 (2014).

74. Case, T. J. On the evolution and adaptive significance of postnatal growth rates in the terrestrial vertebrates. *Q. Rev. Biol.* **53**, 243-282 (1978).

75. Zullinger, E. M., Ricklefs, R. E., Redford, K. H. & Mace, G. M. Fitting sigmoidal equations to mammalian growth curves. *J. Mammalogy.* **65**, 607-636.

76. Oaks, J. R. A time-calibrated species tree of Crocodylia reveals a recent radiation of the true crocodiles. *Evolution.* **65**, 3285-3297 (2011).

77. Smaers, J. B. & Rohlf, F. J. Testing species' deviation from allometric predictions using the phylogenetic regression. *Evolution.* **70**, 1145-1149 (2016).

78. Benton, M. J., Donoghue, P. C., Asher, R. J., Friedman, M., Near, T. J. & Vinther, J. Constraints on the timescale of animal evolutionary history. *Palaeontol. Electron.* **18**, 1-106 (2015).

79. Jenkins, F. A. & Parrington, F. R. The postcranial skeletons of the Triassic mammals *Eozostrodon*, *Megazostrodon* and *Erythrotherium. Phil. Trans. R. Soc. Lond. B.* **273,** 387–431 (1976).

80. Grau, G. A., Sanderson, G. C. & Rogers, J. P.1970. Age determination of raccoons. *The J. Wildlife Management.* 34, 364-372 (1970).

81. Gasawey, W. C., Harkness, D. B. & Rausch, R. A. Accuracy of moose age determinations form incisor cementum layers. *J. Wildlife Management.* **42**, 558-563 (1978).

82. Klevezal, G. A. & Pucek, Z. Growth layers in tooth cementum and dentine of European bison and its hybrids with domestic cattle. *Acta Theriol.* **32**, 115-128 (1987).

83. Kay, R. F. & Cant, J. G. Age assessment using cementum annulus counts and tooth wear in a free-ranging population of *Macaca mulatta. Am. J. Primatology.* **15**, 1-15 (1988).

84. Cederlund, G., Kjellander, P. and Stålfelt, F. Age determination of roe deer by tooth wear and cementum layers-tests with known age material. In Csányi, S. &

Ernhaft, J. (Eds). *Transactions of the 20th Congress of the International Union of Game Biologists, Gödöllö* (540-545). University of Agricultural Sciences. Gödöllö, Hungary (1991).

85. Bodkin, J.L., Ames, J.A., Jameson, R.J., Johnson, A.M. and Matson, G.M. Estimating age of sea otters with cementum layers in the first premolar. *J. wildlife management*. **61**, 967-973 (1997).

86. Landon, D.B., Waite, C.A., Peterson, R.O. and Mech, L.D. Evaluation of age determination techniques for gray wolves. *J. wildlife management.* **62**, 674-682 (1998).

87. Christensen-Dalsgaard, S.N., Aars, J., Andersen, M., Lockyer, C. and Yoccoz, N.G. Accuracy and precision in estimation of age of Norwegian Arctic polar bears (*Ursus maritimus*) using dental cementum layers from known-age individuals. *Polar Biology*. **33**, 589-597 (2010).

88. Pasda, K. Assessment of age and season of death of West Greenland reindeer by counting cementum increments in molars. *Documenta Archaeobiologiae.* **4**, 125-140 (2006).

89. Pérez-Barbería, F.J., Duff, E.I., Brewer, M.J. and Guinness, F.E. Evaluation of methods to age Scottish red deer: the balance between accuracy and practicality. *J. Zool*. **294**, 180-189 (2014).

Acknowledgements

Author Contributions

IJC & PGG conceived and designed the project. EN, PGG, PB, KR & IJC selected, prepared and curated specimens. EN, PGG, PB, VF, DH, TK, AK, FM, AP, BP, PS, HS, PT & IJC performed the synchrotron experiments. EN, AK & IJC performed the microCT experiments. EN processed and EN, CN & KY analysed the synchrotron data. EN & IJC analysed the micro-CT data. EN, PGG & IJC discussed the interpretations. EN wrote the first draft and created all figures; EN, PGG & IJC wrote the manuscript; all authors provided a critical review of the manuscript and approved the final draft. This article originated as a Masters thesis (University of Bristol), then a Ph.D. thesis (University of Southampton), performed by EN and supported and supervised by PGG, PS, NJG, JJ, KRB, MJB & IJC.

Competing interests

The authors declare no competing interests.

Materials and correspondence

Correspondence and material requests should be addressed to Elis Newham, Pam Gill, and Ian Corfe.